A Broadband Acoustic Technique for Measuring Bubble Size Distributions: Laboratory and Shallow Water Measurements

ERIC J. TERRILL AND W. KENDALL MELVILLE

Scripps Institution of Oceanography, University of California, San Diego, La Jolla, California

(Manuscript received 28 January 1998, in final form 28 December 1998)

ABSTRACT

The development of a broadband sound velocimeter that allows the simultaneous measurement of sound speed and attenuation over a wide range of frequencies is described. The velocimeter measures the attenuation and dispersion of a broadband acoustic pulse over frequencies ranging from 4 to 100 kHz across a fixed pathlength using a two-transducer system. The resulting data are inverted to arrive at bubble size distributions over bubble radii in the range 30–800 μm.

The instrument was tested in the large wave channel at the Hydraulics Laboratory of Scripps Institution of Oceanography. The channel can generate breaking waves of O(1 m) height using a hydraulically driven wave generator, giving bubble size distributions similar to those found in the field. The presence of the bubbles significantly changes the acoustical properties of the water. Internal consistency checks of the acoustic data and measurements of bubbles using an independent optical sizing technique support the accuracy of the acoustic system in measuring bubble size distributions.

A field test of the system was performed off Scripps Pier in water of approximately 6-m depth. Observations demonstrate that bubble transport events with significant temporal and spatial variability are associated with rip currents and introduce significant vertical gradients in the acoustical properties of the water. The performance of the system in the field was found to be comparable to that found in the laboratory.

1. Introduction

A number of acoustic and optical techniques have been developed to measure oceanic bubble populations to better understand the role of bubbles in air–sea interaction and ocean acoustics. Measurements by previous investigators have revealed significant variability in the bubble size distributions near the ocean's surface. This variability has been attributed to a combination of deficiencies in the measurement techniques and the variability of the ocean's near-surface bubble field that results from intermittent wave breaking events. To better understand the distribution of bubbles in the ocean, measurements are required that span a wide range of oceanographic conditions with sufficient temporal resolution to prevent aliasing with wave breaking events. The measurement technique should also be tested with independent measurements to avoid artifacts of instrument performance.

Field measurements of bubble size distributions using optical techniques have generally been limited to some form of manual counting (Blanchard and Woodcock 1957; Medwin 1970; Kolovayev 1976; Johnson and Cooke 1979). Due to the time intensive nature of analyzing the data, the studies have been of short duration. The results obtained by Johnson and Cooke (1979) are typically accepted as the most accurate of the optical datasets obtained beneath breaking waves, despite some shortcomings of the technique. The data were obtained with a floating camera system modeled after the design used by Medwin (1970) in his studies of bubble populations found in low sea states. The camera system used by Johnson and Cooke (1979) was suspended from the ocean surface and images were obtained at 30-s intervals. Recent developments in the field of image processing have led to an optical technique designed by Geissler and Jahne (1997a,b), which measures bubbles at much higher sampling rates in a sampling volume that is well defined by the depth of focus of the optics.

The acoustical properties of bubbles provide a variety of approaches to measure the bubble size distribution, many of which have been pioneered by Medwin and his students (Medwin 1970, 1977; Medwin et al. 1975; Medwin and Breitz 1989). Determination of both the acoustic phase speed and attenuation by bubbly water was accomplished by the measurement of sound propagation across a fixed pathlength as well as the interpretation of the spectral response of a flooded acoustical resonator. One result of their efforts has been the sub-

Corresponding author address: Eric J. Terrill, Scripps Institution of Oceanography, 8605 La Jolla Shores Drive, Mail Stop 0230, La Jolla, CA 92093.
E-mail: et@mpl.ucsd.edu

sequent refinement of a number of their techniques by other investigators (Su et al. 1994; Lamarre and Melville 1995; Farmer and Vagle 1997) as newer technology, advanced signal processing techniques, and improved acoustic inversion schemes have become available. The work of Farmer and Vagle (1997) on Medwin's original resonator design has resulted in a number of improvements, including the removal of hydrostatic pressure effects through the use of PVDF transducers and the implementation of real-time processing that allows data acquisition at rates of $O(1)$ Hz. Progress in the analysis of the resonator's response to a bubbly medium now provides for internal consistency checks on the acoustic data.

This paper presents the development, testing, and examples of data obtained from a two-transducer sound velocimeter. The technique measures phase speed and attenuation across a band of frequencies ranging from 4 to 100 kHz through the use of a broadband pulse. Advances in data acquisition and storage permit measurements to be made at rates up to 12 Hz, allowing the determination of bubble size distributions with high temporal resolution. In section 2 of this paper, a review of the physics of sound propagation through a bubbly medium and the various bubble size inversion techniques available are presented. Section 3 describes the hardware and signal processing of the transducer system and defines the range of bubble densities in which the system can operate. Section 4 presents the results of a series of tests made beneath breaking waves in the laboratory. Section 5 outlines the performance of the system during a field test in shallow water.

The work described in the paper follows from the earlier work of Lamarre and Melville (1994) who reported sound speed measurements made at 6–40 kHz using a broadband pulse. Preliminary results of the development and results reported in this paper have previously appeared in Melville et al. 1996, 1997), Terrill and Melville (1996, 1997a,b, 1998), and Terrill (1998). Since this paper was originally submitted for publication, Vagle and Farmer (1998) have published a review of methods to measure bubble size distributions, which include the method described here.

2. Sound propagation through a bubbly medium

Bubbles are known to have a characteristic radial resonant frequency, approximated by

$$\omega_0 = \frac{1}{a}\left(\frac{3\gamma P_{\text{amb}}}{\rho_w}\right)^{1/2}, \tag{1}$$

where $\gamma = c_p/c_v$ is the ratio of the specific heats of the entrained gas, ρ_w is the density of pure water, a is the radius, and P_{amb} is the ambient pressure in the bubble. The approximation deviates from the true resonant frequency for small radii due to the role of surface tension and a shift in the thermodynamics of the gas from adiabatic to isothermal conditions. However, the correction is small, with an error of only 5% for a bubble with a 30-μm radius at sea level (Clay and Medwin 1977). Because of resonant effects, the scattering and absorption cross sections of bubbles are 10^3–10^4 times their geometrical cross sections at frequencies near resonance. Furthermore, the bubble is unable to oscillate in phase when forced by incident sound waves near the bubble's resonant frequency, introducing phase shifts in the sound propagating through the medium. [See Leighton (1994) for a discussion of forced bubble oscillations].

Commander and Prosperetti (1989) derive the complex dispersion relationship for linear wave propagation and attenuation through a polydisperse population of bubbles as

$$\frac{c^2}{c_m^2} = 1 + 4\pi c^2 \int_0^\infty \frac{an(a)\, da}{\omega_0^2 - \omega^2 + 2ib\omega}, \tag{2}$$

where c is the bubble free sound speed, c_m is the complex sound speed in the mixture, ω_0 is the radial resonant frequency of a bubble of radius a [Eq. (1)], ω is the radian frequency of the sound, b is the damping coefficient, and $n(a)da$ is the number of bubbles per unit volume in the range $(a, a + da)$. Typically, $n(a)$ is reported as the number of bubbles per m^3 per micron radius increment (which will be used throughout this paper). When integrated over all bubble sizes present in the mixture, the real and imaginary parts of the complex sound speed describe the phase speed and attenuation of sound propagating through the medium. The integral form of (2) is equivalent to the results of Foldy (1945), who showed that in a dilute mixture of scatterers, the total scattering is equal to the sum of the individuals, implying that the pressure fields of individual bubbles do not interact. Commander and Prosperetti (1989) showed that the linearized bubble model compares well with a number of historical measurements that contain a wide range of radii at void fractions up to 1%. At much higher void fractions the effects of multiple scattering become significant and the assumptions in the derivation of (2) are no longer valid. Readers are referred to Commander and Prosperetti (1989) [see also Waterman and Truell (1961), Leander (1994), Feuillade (1996)] for a discussion of the various criteria that have been derived for neglecting multiple scattering effects.

While the Foldy approximation places a restriction on the use of (2) to describe acoustic propagation in very dense bubble clouds, field measurements have shown that high void fractions of $O(10^{-1}$–$1)$ that exist directly beneath breaking waves in the ocean will quickly degas over timescales of a wave period or less to bubble densities suitable for acoustic sizing techniques, which neglect multiple scattering. This is consistent with earlier measurements by Melville et al. (1996), who showed typical mean void fractions in the upper ocean

ranging from 10^{-7} to 10^{-4} in steady winds of approximately 13 m s^{-1}.

An example of the attenuation and phase speed as a function of frequency, obtained from Eq. (2), is given in Fig. 1 for two different size distributions of bubbles. The two distributions in Fig. 1c are a power law, with a slope of -3.5 (solid line) between $a = 30$ and 600 μm, and a narrow distribution centered at 60-μm radius (dashed line). The number densities of the bubble populations were determined by setting the void fractions for both distributions to $\beta = 1.91 \times 10^{-7}$. The resulting frequency-dependent attenuation curves are shown in Fig. 1b. The narrow distribution gives large attenuation in a narrow frequency band centered at the resonant frequency of a 60-μm bubble, while the power-law relationship exhibits attenuation across a wider frequency band that corresponds to the wider range of radii present in its distribution. Figure 1c shows that there are three different regimes for the phase speed that are common to both distributions. At frequencies much greater than the resonant frequencies of the bubbles present, the phase speed asymptotes to the value for bubble-free water. The region of dispersion is noted by the region of strong frequency dependence and varies according to the range of bubble sizes and the shape of the size distribution. At frequencies much lower than the resonant frequencies of the bubbles the phase speed becomes nondispersive. In the low frequency limit, the sound speed c_m is a function of the density ρ_m and compressibility K_m of the mixture, given by

$$c_m = \frac{1}{(\rho_m K_m)^{1/2}}, \tag{3a}$$

where

$$\rho_m = \beta\rho_a + (1 - \beta)\rho_w \quad \text{and} \tag{3b}$$

$$K_m = \beta K_a + (1 - \beta)K_w. \tag{3c}$$

Here, K_a and K_w are the compressiblity of air and water, respectively. In this limit the sound speed is simply a function of the void fraction β (Wood 1941). This relationship provided the basis for the development of a single frequency sound velocimeter by Lamarre and Melville (1995) to make measurements of entrained air beneath breaking waves. Propagation times of a narrowband acoustic pulse across a fixed pathlength were measured, providing a direct measurement of the sound speed. The technique was used by Terrill and Melville (1997a,b) for the acquisition of long time series of up to seven weeks on moored instruments and proved to be robust (Terrill 1998).

To invert the acoustical properties of the bubbly mixture to give the size distribution of bubbles present, we consider the complex wavenumber given by the dispersion relation [Eq. (2)]:

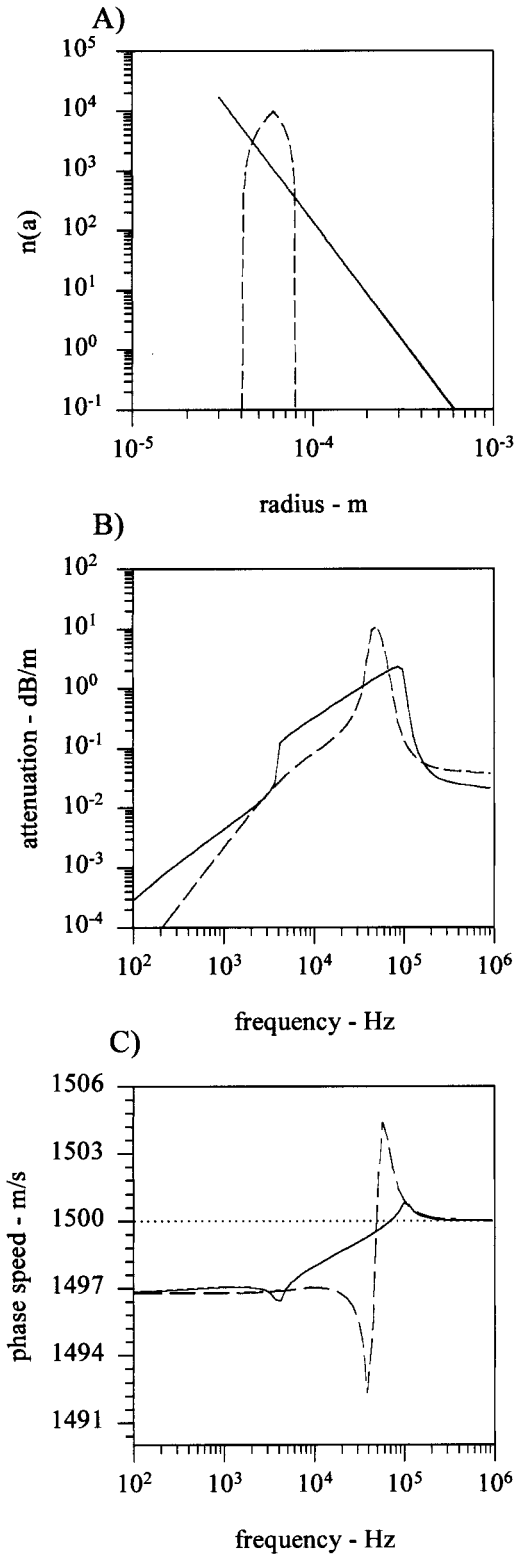

FIG. 1. (a) Two examples of bubble size distributions. The solid line corresponds to a size distribution with a power-law dependence of slope -3.5. The dashed line is a narrowband distribution centered at a radius of 60 μ. The void fractions for both distributions are set equal to 1.91×10^{-7}. (b) The frequency-dependent attenuation and (c) dispersion curves that result from the two different distribution of bubbles.

$$k_m^2 = \frac{\omega^2}{c^2} + 4\pi\omega^2 \int_0^\infty \frac{an(a)\, da}{\omega_0^2 - \omega^2 + 2ib\omega}, \quad (4)$$

where the acoustic pressure is given by

$$p = P_0 e^{-k_i x} e^{i(\omega t - k_r x)}. \quad (5)$$

Solving for both the real and imaginary parts of the wave number through the use of a Taylor series expansion of Eq. (4) [ignoring terms of $O(k^2)$] gives (Clay and Medwin 1977; Leighton 1994)

$$k_r = k_w \left(1 + 2\pi \int \frac{an(a)}{k_r^2} \frac{\left(\frac{\omega_0}{\omega}\right)^2 \left(\left(\frac{\omega_0}{\omega}\right)^2 - 1\right)}{\left[\left(\left(\frac{\omega_0}{\omega}\right)^2 - 1\right)^2 + \delta^2\right]} da \right) \quad (6)$$

and

$$k_i = k_w \left(2\pi \int \frac{an(a)}{k_r^2} \frac{\left(\frac{\omega_0}{\omega}\right)^2 \delta}{\left[\left(\left(\frac{\omega_0}{\omega}\right)^2 - 1\right)^2 + \delta^2\right]} da \right), \quad (7)$$

where k_w is the acoustic wavenumber in pure water. The attenuation of the acoustic signal, expressed in units of decibels per unit length, is then given by

$$\alpha(\omega) = 10 \log_{10}(e) \int \frac{4\pi a^2 (\delta / k_r a) n(a)}{\left(\left(\frac{\omega_0}{\omega}\right)^2 - 1\right)^2 + \delta^2} da \quad \text{or} \quad (8)$$

$$\alpha(\omega) = 4.34 \int_0^\infty \sigma_e(\omega, a) n(a)\, da, \quad (9)$$

where σ_e is defined as the extinction cross section of a bubble of radius a at an ensonifying frequency ω. The extinction cross section represents the power scattered and absorbed by a single bubble when exposed to an external pressure field.

Equation (9) is a Fredholm integral equation of the first kind. The earliest inversion of attenuation data for bubble size distributions is that by Wildt (1946) in his measurements of excess attenuation of sound propagation through a bubbly ship wake. To simplify the inversion of Eq. (9), it was assumed that only bubbles with a resonant frequency corresponding to the frequency of interest contributed to the attenuation. This ''resonant approximation'' eliminated the need for inverting the integral and provided an explicit solution for the numberper unit volume of bubbles whose radius (a_r) resonated when driven by a frequency as defined by Eq. (1):

$$n(a) = \frac{\alpha(\omega) k_r}{85.7 a_r^2} \quad (10)$$

(Wildt 1946; Clay and Medwin 1977).

Commander and McDonald (1991) have proposed a direct numerical solution to Eq. (9) using a simple finite-element method incorporating a system of linear equations generated using splines for the element shape functions. Singular value decomposition is then used to solve the ill-conditioned linear system. A regularization procedure, which subjects the solution to a minimum curvature constraint, stabilizes the system of equations. This inverse method is an improvement over the resonant approximation as it corrects for the effects of off-resonant bubbles. Off-resonant bubbles can introduce errors in the resonant approximation to the solution of Eq. 9 when a wide range of bubble radii are present in the acoustic field. The errors are a result of the off-resonant extinction cross section of larger bubbles approaching or exceeding the resonant extinction cross section of small bubbles (Commander and Moritz 1989; Commander and McDonald 1991). These authors have shown that by including off-resonant effects and directly solving the integral equation, their inversion technique is able to accurately reproduce data for a number of assumed bubble distributions over a wide range of radii.

Recently, Duraiswami (1993) proposed an inversion technique, which uses kernels obtained from both the real (6) and imaginary (7) parts of the wave number. The void fraction and total surface area of the bubbles are used as physical constraints that are imposed on the solution and a linear optimization approach incorporating the simplex method is used to solve the resulting inversion problem. The method has been used on field data at frequencies from 6 to 40 kHz. The technique was found to be computationally intensive and was not deemed appropriate for processing the large amounts of data that would be generated by the broadband technique in field applications.

The suitability of using the steady-state dispersion relation, given by Eq. (2), for the interpretation of transient pulse transmissions through bubbly water must be considered. The investigation of acoustic backscatter by Akulichev et al. (1986) suggested that the time dependence of the resonant portion of the acoustic cross section to ''ring up'' could be modeled using a simple exponential form

$$\sigma_e = \sigma_{\text{nr}} + (1 - e^{-2t/t_0})\sigma_r, \quad (11)$$

where σ_{nr} is the nonresonant cross section, σ_r is the resonant cross section, and t_0 is the time required for the bubble to undergo Q/π oscillations. Here, Q is the well-known quality factor related to the resonance of a bubble and is equal to the inverse of the damping coefficient $\delta = 2b/\omega$. Expression (11) suggests that pulsed transmission measurements in bubbly water would require pulse lengths comparable to or greater than t_0 to invert the steady-state dispersion relation [Eq. (2)] for bubble sizes. However, recent laboratory work by Pace et al. (1997) on the acoustic excitation of bubble mixtures suggests that the forward transmission loss of sound through a bubbly medium is independent of pulse

length for lengths greater than one cycle (much less than t_0). Their work compared the attenuation of 20-cycle-long pulses with short pulses ranging from one to four cycles over a frequency range of 20–200 kHz and found no dependence of transmission loss on pulse length in this range. This work supports earlier laboratory work by Suiter (1992), who looked at the pulse length dependence of 120-kHz sound propagation in bubbly water. The author found that pulses of 2.6 cycles in duration exhibited no differences in attenuation when compared with pulses 6–20 cycles in length. Both sets of measurements suggest that short pulse propagation through a collection of bubbles is much less sensitive to pulse length than the theory of Akulichev et al. (1986) would imply. While heuristic arguments have been proposed by the authors to explain their results, including effects of multiple scattering within the bubble cloud and the suggestion that the excitation of a bubble to acoustic resonance is triggered much faster than described by the exponential dependence in Eq. (11), no complete theoretical treatment that explains their findings is readily available in the literature. The bubble size inversions presented in this paper assume that the steady-state bubble dispersion relation is valid for the pulse lengths used and that the damping coefficients of the bubbles are given by the theory of Devin (1959) and Clay and Medwin (1977).

The form of the complex dispersion relation given by Eq. (2) and inversions of Eq. (9) introduce a relationship between the phase speed, attenuation, and the bubble size distribution. Specifically, knowledge of the attenuation for a number of different frequencies allows the calculation of the phase speed once the inversion for bubble sizes has been performed. This relationship is useful in evaluating the performance of the broadband acoustic technique presented here since both the phase speed and attenuation are measured directly. This will be considered in a later section when discussing the performance of the broadband technique.

3. Instrument development

a. Acoustic pulse design

Measurement of the phase speed and attenuation is accomplished through the transmission of a broadband pulse transmitted across a fixed pathlength. Uncertainty in previously reported bubble size distributions gave uncertain guidance in predicting which frequency bands would experience the largest attenuation and it was decided to use a system with a relatively flat spectral response across the frequency band 4–100 kHz, which corresponds to bubble radii in the range of approximately 30–820 μm. A pulse with a flat spectral response is desirable as the full dynamic range of the analog-to-digital converter can then be utilized. As discussed by Lamarre and Melville (1994), if performing measurements some distance d from a boundary using a pulsed

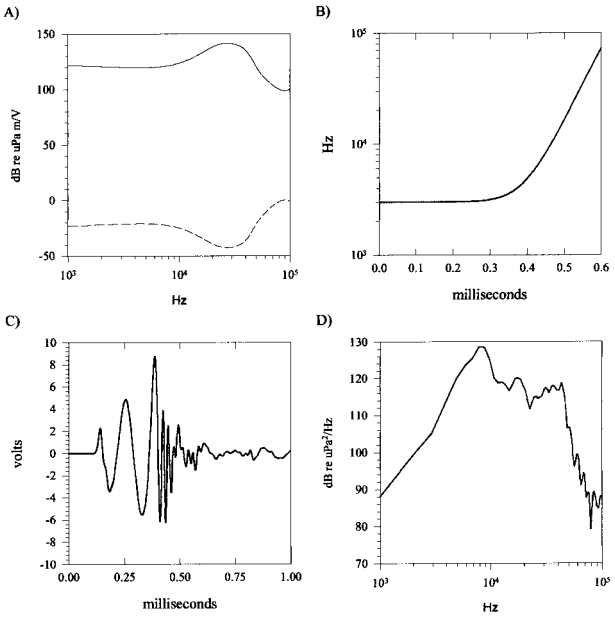

FIG. 2. (a) Transmit voltage response curve for an I.T.C. 1032 spherical transducer (solid line) and its complementary amplitude correction curve $A(f)$ (dashed) that is used for producing a pressure wave with fixed amplitude across the band of frequencies shown. (b) The frequency sweep $f(t)$ used in the design of the broadband pulse. (c) Time series of the broadband pulse as received by the I.T.C. 1042 hydrophone in bubble-free water. (d) The power spectrum of the received broadband pulse in units of decibels relative to 1 μPa^2 Hz^{-1}.

acoustic technique, the pulse length L_p, and propagation distance L_d must be balanced so that multiple arrivals will not bias the measurements. This minimum distance can be determined geometrically to be

$$d = \left[\left(\frac{L_p + L_d}{2}\right)^2 + \left(\frac{L_d}{2}\right)^2\right]^{1/2}. \qquad (12)$$

Use of a pulse whose length was approximately 0.6 ms in duration allows the system to operate at distance of 52 cm from boundaries for an acoustic pathlength of 15 cm. To implement the pulse, an I.T.C. 1032 spherical transducer (68.5-mm diameter) was chosen for its output response level and resonant frequency. Due to the frequency response of the transducer, an amplitude correction factor as a function of frequency, $A(f)$, was used to allow the design of a pulse with relatively flat frequency response. Figure 2a shows the frequency-dependent transmit voltage response curve of the transducer and the corresponding amplitude correction used.

A frequency-swept signal, $\sin[2\pi f(t)t]$, was used to design the pulse shape. Initially, a linear sweep rate (df/dt = constant) was used, but it was found that sufficient power could not be transmitted at the lower frequencies without requiring the total pulse duration to be significantly longer. To provide sufficient power at the lower frequencies and retain a pulse length of 0.6 ms, a nonlinear sweep rate was finally used. The frequency sweep used is shown in Fig. 2b. Combining the

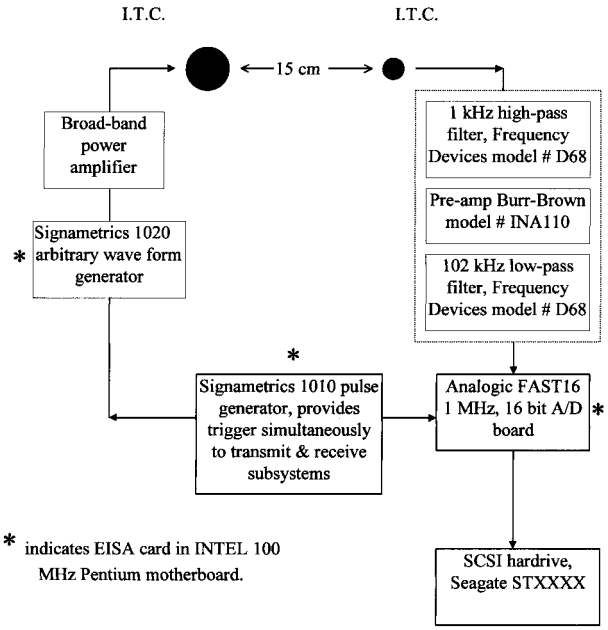

FIG. 3. Block diagram of the electronic hardware for the broadband velocimeter. Boxes with an asterisk indicate they are EISA plug-in cards on the 100-MHz Pentium motherboard.

transducer amplitude correction and sweep rate, the form of the electrical signal sent to the transducer is

$$v(t) = A[f(t)] \sin[2\pi f(t)t]. \quad (13)$$

A lookup table was created for the amplitude correction factor $A(f)$. The shape of the received pulse, as measured by the system in bubble-free water, is shown in Fig. 2c. Due to the phase response of the spherical transducer, the signal does not appear as a clean FM sweep. The phase response of the transducer was not considered relevant in the design of the pulse shape because relative phase delays between one frequency and another within the pulse are not important as long as the pulse is repeatable.

In order to specify the amplitude of the acoustic pulse, the ambient noise field and the expected levels of attenuation of the pulse are considered. Ambient noise levels in the ocean have been studied for quite some time (Kerman 1988, 1993) and are known to increase with the wind speed and to contain a peak at O(500–1000) Hz with a frequency-dependent rolloff of approximately 17–20 dB per decade. For example, at a wind speed of 20 m s^{-1}, the ambient noise level is approximately 70 dB relative to 1 μPa^2 Hz^{-1} at 500 Hz. Noise levels beneath individual breakers can be expected to be several decibels higher (Farmer and Vagle 1989). Both historic data (Silberman 1957; Fox et al. 1955) as well as simple modeling efforts, like the curves shown in Fig. 1b, suggest that attenuation levels of O(100) dB m^{-1} or more could be expected, depending on the bubble size distribution present. In light of these high attenuation levels, it is unrealistic to attempt measurements across O(1) m in large concentrations of bubbles. If O(0.1)-m pathlength is used, the expected excess attenuation due to bubbles across the pathlength would be only O(10) dB, which is a significant improvement. The importance of accurate attenuation measurements is shown by considering the sensitivity of the ''resonant approximation'' bubble inversion [Eq. (10)], where an attenuation of 1 dB m^{-1} at 100 kHz (bubble radius of 30 μm) translates to a bubble density of approximately

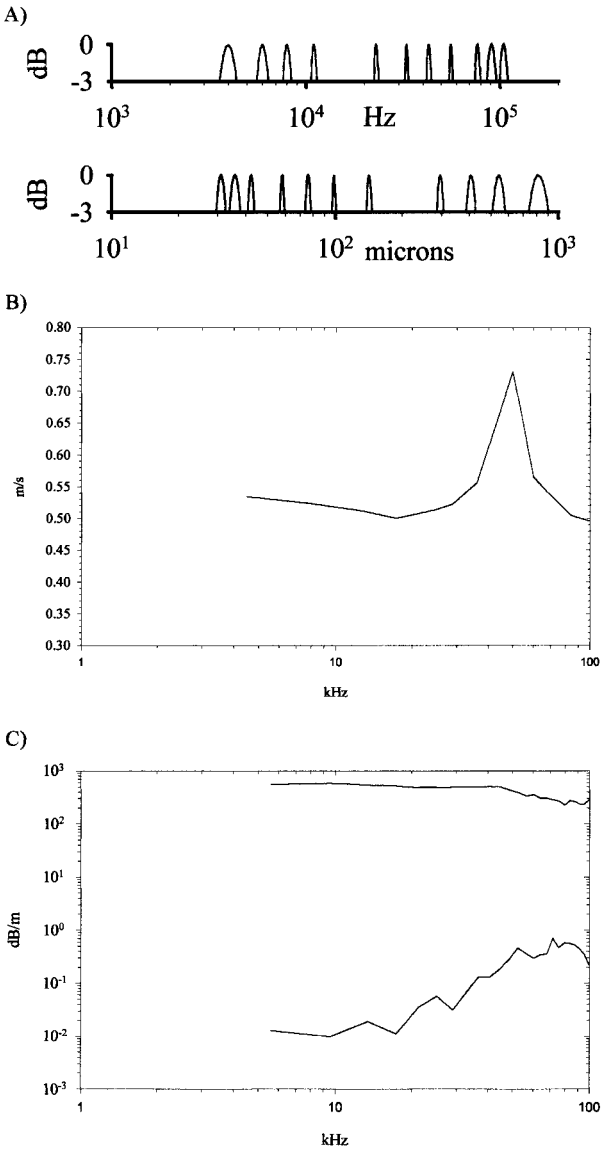

FIG. 4. (a) The −3-dB frequency response (and the corresponding resonant bubble sizes) of the digital filters used for calculating the phase speed. (b) The standard deviation of the sound speed measurement as a function of frequency. Calculations are based on data obtained by operating the sound speed module in bubble-free water. (c) The maximum and minimum attenuation levels (units of dB m^{-1}) the system is able to resolve as a function of frequency. The minimum level is based upon data obtained by operating the module in bubble-free water.

4600 m^{-3} μm^{-1}. An I.T.C. 1042 hydrophone was chosen as the receiver for its wideband (1 Hz–120 kHz), flat response (−198 dB re 1 V μPa^{-1}) and small dimension (34.9-mm diameter). An example of the received power spectrum of a single pulse propagated across 15 cm in bubble-free water is shown in Fig. 2d. The levels shown are sufficiently above the expected ambient noise field, providing good dynamic range for a wide range of attenuation levels. Furthermore, the transmitted pressure level of *O*(1000) Pa is much less than the total ambient hydrostatic pressure so that the bubbles can be assumed to behave with small amplitude oscillations, a necessary assumption in the linear theory of bubble acoustics.

b. Hardware and software

Block diagrams of the transmit and receive subsystems are shown in Fig. 3. To begin operation, a system initialization is performed that loads the predetermined transmit pulse from the system's hard drive to the onboard RAM of the arbitrary waveform generator. A communications check is also performed between the various components of the system. Once initialized, the system enters an online mode where it awaits a trigger to begin its transmit and receive routine. The pulse generator synchronizes the two subsystems, providing a trigger simultaneously to the two. When triggered, the broadband pulse signal is amplified and transmitted through the transmit transducer to the receiver located 15 cm away. When the pulse is received, it passes through a custom signal conditioning board (dashed box) that contains both amplifiers and antialiasing filters. The signal is then digitized at 16-bit resolution at a 1-MHz rate by the A/D card (Analogic FAST-16) for 2048 ms and written to an SCSI hard drive. A high quality hard drive, such as the Seagate model number ST32550N currently used by the system, can store the raw acoustic data at a ping rate of up to 12 Hz during continuous operation. The ping rate was limited by the write speed of the hard drive, which varies by model and manufacturer. While some preprocessing of the data could be performed to reduce the storage requirements, it was decided to assess the raw data offline to allow a complete evaluation of the system.

In order to calculate the phase speed and attenuation as a function of frequency, the received broadband signal is discretized into a number of narrowbands. This is accomplished using 12 narrowband finite impulse response (FIR) digital filters logarithmically spaced from 4–100 kHz. The half-power (−3 dB) frequency response of the digital filters is shown in Fig. 4a with the corresponding resonant bubble radius. Once the signal is filtered, the data are compared with similarly filtered reference signals obtained in bubble-free water. The time delay is calculated using the cross correlation of the data with the reference signal obtained in bubble-free water. The time resolution of the delay is improved by *O*(10) through the use of a spline fit to the cross-correlation peak, as described by Lamarre and Melville (1995). Estimates of the standard deviation of the time delay measurement can be evaluated through the Cramer–Rao lower bound (Quazi 1981; Lamarre and Melville 1995). This lower bound is a function of the signal-to-noise ratio (SNR), observation time, and signal bandwidth. Since the level of the acoustic pulse is much higher than the ambient noise field, the SNR of the system is determined by the electrical noise floor of the system, resulting in an SNR of approximately 3300 (70 dB). The estimated lower bound, based on the Cramer–Rao relation, is calculated to be equivalent to a sound speed accuracy of 0.1 m s^{-1}. This value was found to agree with the standard deviation of the system's ability to measure sound speed. The system was tested in water

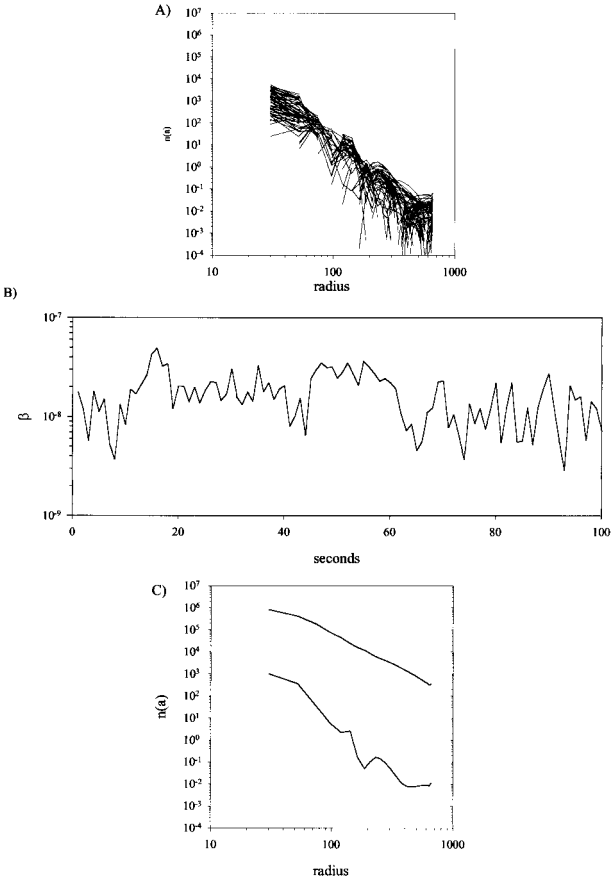

FIG. 5. (a) The bubble size distributions that result from inverting attenuation levels that occur due to system electrical noise. The attenuation levels were obtained by operating the system in bubble-free water at a 1-Hz ping rate and measuring the effects of low-level noise on the received signal. (b) Time series of the void fraction of the equivalent bubble size distributions [shown in (a)] that are a result of the noise. The mean void fraction is 1.73×10^{-8}, defining the lower limit of the void fraction range the system can measure. (c) The range of bubble densities the system can resolve based upon the attenuation measurement limits. The lower bubble size distribution is the mean of the distributions shown in (a), while the upper limit is the distribution that is a result of inverting the upper limit on the attenuation level shown in Fig. 4c.

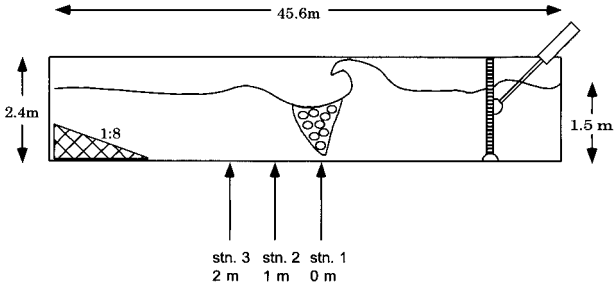

FIG. 6. Schematic of the large wave channel at the Hydraulics Laboratory, Scripps Institution of Oceanography. Breaking waves can be formed in the channel through the use of a dispersive wave packet technique (Rapp and Melville 1990). Measurements were made with the broadband velocimeter at the three stations indicated. The channel was filled with seawater so that the bubble size distributions measured would be similar to those found in the field.

of a known sound speed, as determined by accurate measurements of temperature and salinity (Medwin 1975). The standard deviation of the sound speed measurement was calculated across the frequency band and found to be in the range 0.5–0.75 m s^{-1} (as shown in Fig. 4b).

The excess attenuation due to bubbles, α, expressed in units of decibels per meter is obtained through the use of

$$\alpha = \frac{10}{l}\log\left(\frac{P^2}{P_0^2}\right), \tag{14}$$

where l is the signal pathlength, P_0 is the received acoustic pressure in bubble-free water, and P is the measured pressure. The pressure levels can be obtained by calculating the rms acoustic pressure in each filtered band. A similar method involves the comparison of the power spectra of the broadband pulse with a reference pulse spectra obtained in bubble-free water. The spectral technique is advantageous as it provides higher frequency resolution with fewer computational steps, leading to a shorter processing time. A spectral technique involving the phase of the signal was tested for measuring the sound speed but found to be unsuitable due to multiple

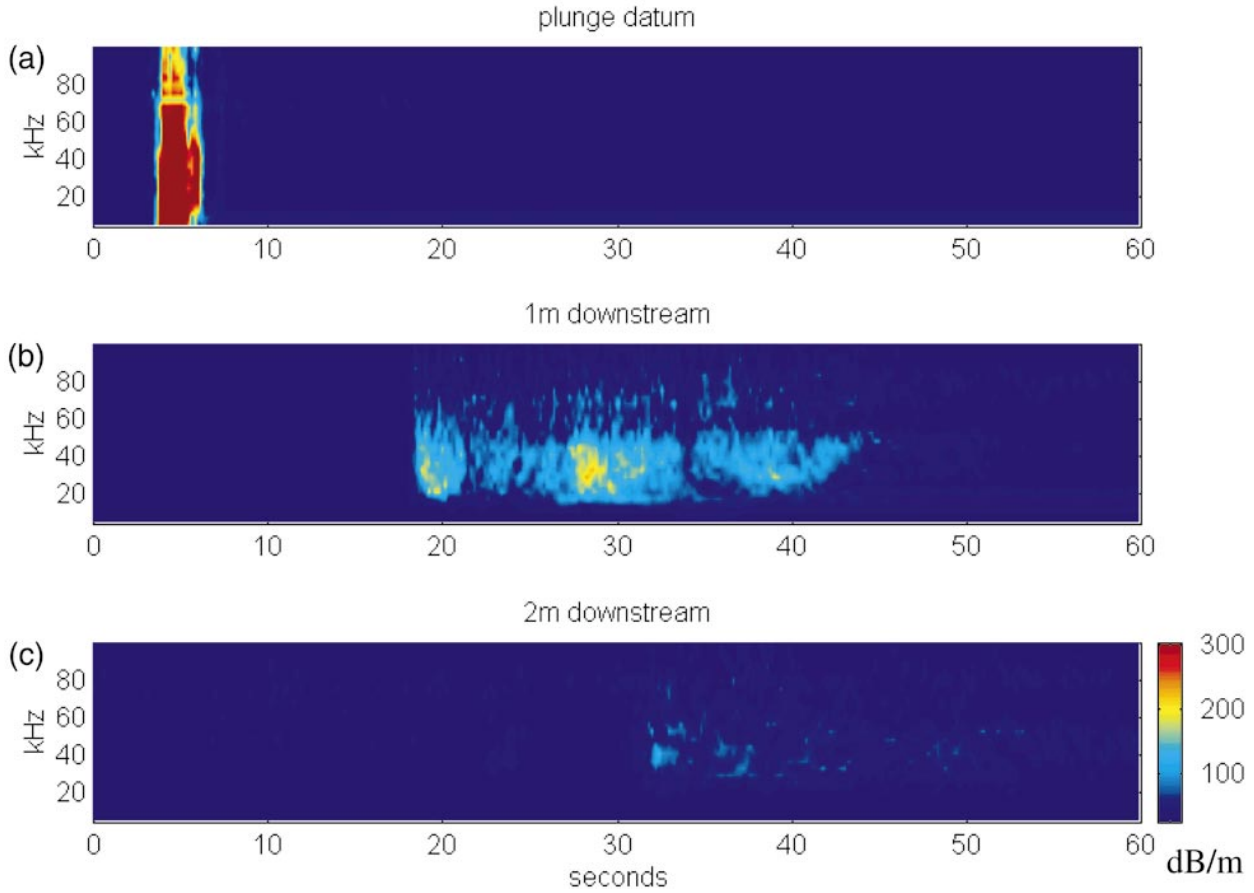

FIG. 7. Color time series of the excess attenuation due to bubbles generated by the laboratory breaking waves in seawater. The x axis is time in seconds, y-axis frequency in kilohertz, and the color intensity represents the attenuation level as referenced by the color scale. Measurements were performed at (a) locations just beneath the breaker and at distances of (b) 1 m and (c) 2 m downstream. Attenuation levels measured just beneath the breaker [see (a)] have saturated the system, indicating that the peak levels shown exceed those defined by the top line in Fig. 4c.

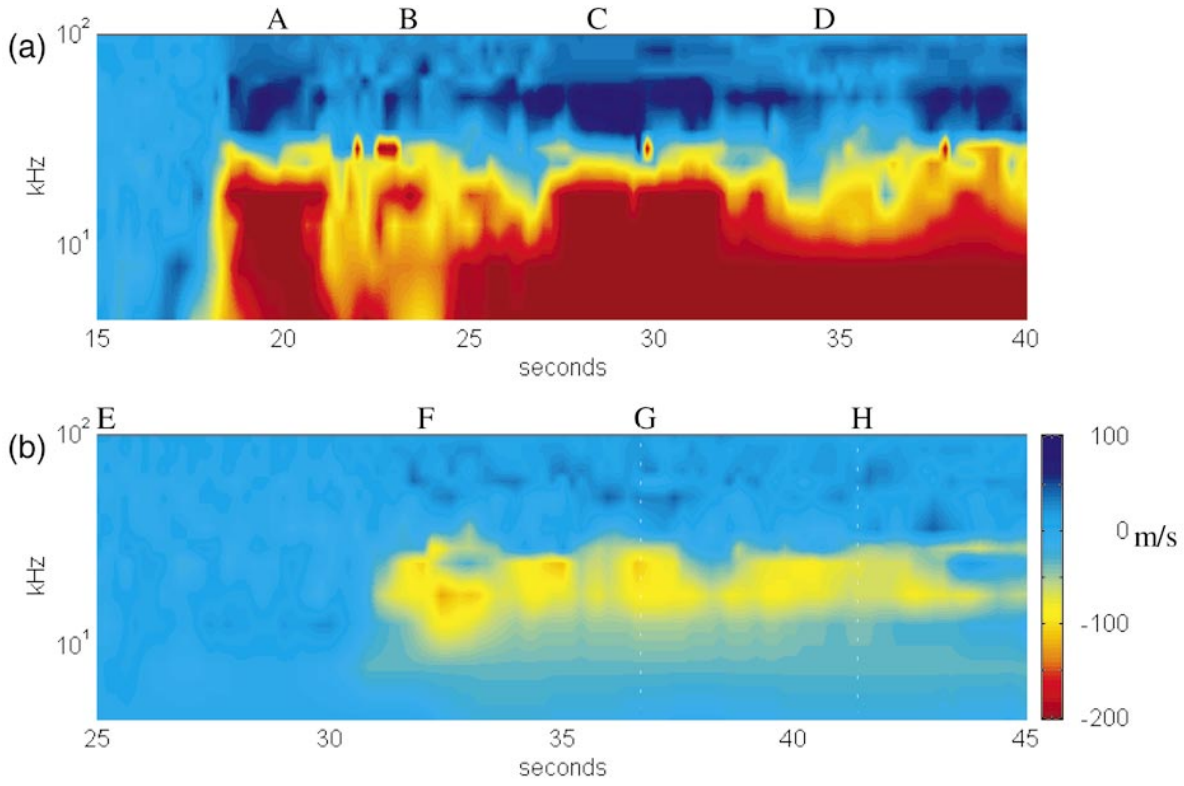

FIG. 8. The color time series of the sound speed anomaly measured while the bubble cloud advects past the transducers. The *x* axis is time in seconds, *y* axis is frequency in kilohertz (log scale), and the color intensity represents the sound speed anomaly. The time axis in (a) and (b) are concurrent with the data shown in Figs. 7b,c. The vertical dashed lines (A–H) represent time periods that are shown in line graph form in Fig. 9.

jumps in 2π that occurred as a result of large sound speed changes. This processing method may hold some promise with the development of a phase unwrapping algorithm.

The range of attenuation levels that the system can measure is determined by examining the levels of noise present in the electronics. This approach is valid since the pulse level is much higher than the ambient acoustic noise field. The maximum attenuation level is defined as the level at which the received acoustic pulse generates a voltage less than or equal to the electrical noise floor of the system. These maximum attenuation levels are shown as a function of frequency as the top line in Fig. 4c. Similarly, very small changes in the received pressure signal must generate voltage levels that exceed the voltage levels generated by electrical noise, defining the minimum attenuation level that can be measured. To assess these minimum attenuation levels, data obtained from operating the system in bubble-free water at a 1-Hz ping rate are evaluated. Fluctuations in the measured attenuation levels arise from low-level electrical noise causing small variations in the received signal. Since the electrical noise is random with respect to the received acoustic signal, the effects of the noise on the system must be determined over a number of pings. The lower solid line shown in Fig. 4c shows the mean attenuation level as a function of frequency measured by the system for data obtained in bubble-free conditions. The effects of the electrical noise on the ability of the system to resolve small attenuation are put into context if the data are inverted for bubble size distributions and the subsequent void fraction is calculated. Figure 5a presents the resulting bubble size distributions obtained applying the attenuation data at the noise floor with the Commander and McDonald (1991) inversion scheme. The void fraction that would be given by these bubble size distributions is shown as a time series in Fig. 5b. The mean void fraction is 1.73×10^{-8}, providing an estimate of the minimum void fraction the system can reliably measure. Figure 5c shows the mean size distribution of the data shown in Fig. 5a as well as the size distribution, which results from inverting the maximum attenuation levels the system can measure (as shown in Fig. 4c). Based on the attenuation limits determined, the range of bubble densities the system can resolve is approximately 3–4 orders of magnitude (radius dependent) and spans a large portion of the expected bubble densities found in the ocean. These densities correspond to a void fraction range of 1.73×10^{-8}–2.4×10^{-4}.

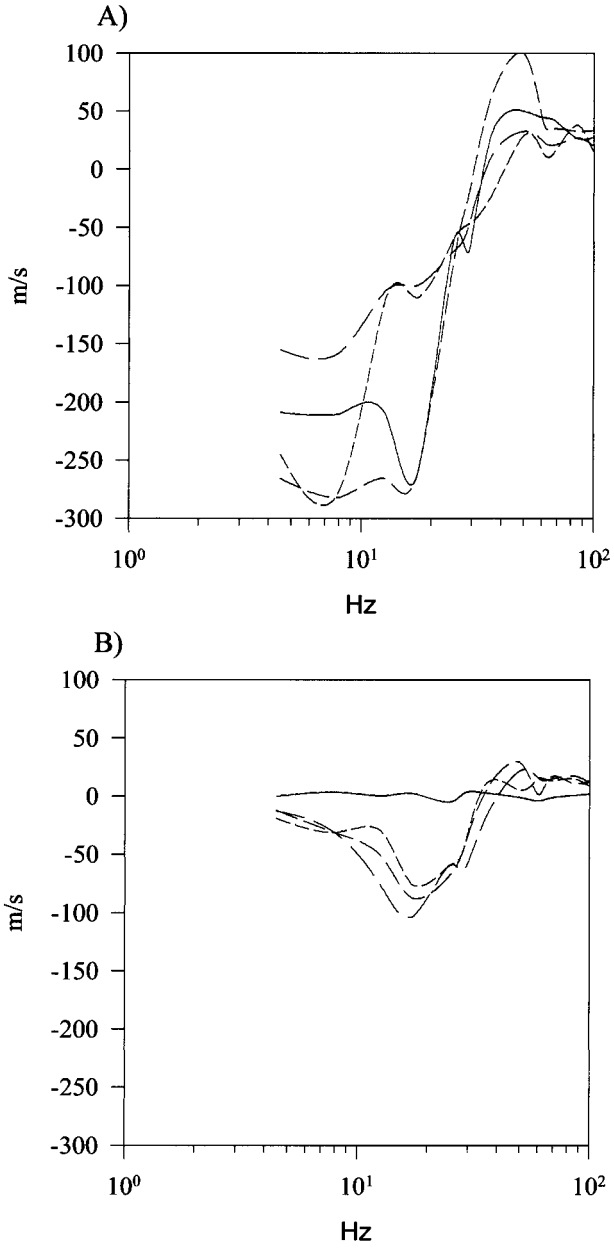

FIG. 9. Representative dispersion curves that are a result of the laboratory-generated bubble cloud advecting past the sound speed module at distances of (a) 1 and (b) 2 m downstream from the onset of breaking. The various line graphs are ''slices'' in time of the color figure shown in Figs. 8a,b, which are denoted by the vertical dashed lines labeled A–H. Times shown in (a) are at $t = 20$ (solid line), 24 (short dash), 28 (medium dash), and 35 s (long dash). Times shown in (b) are at $t = 25$ (solid line), 32 (short dash), 37 (medium dash), and 43 s (long dash).

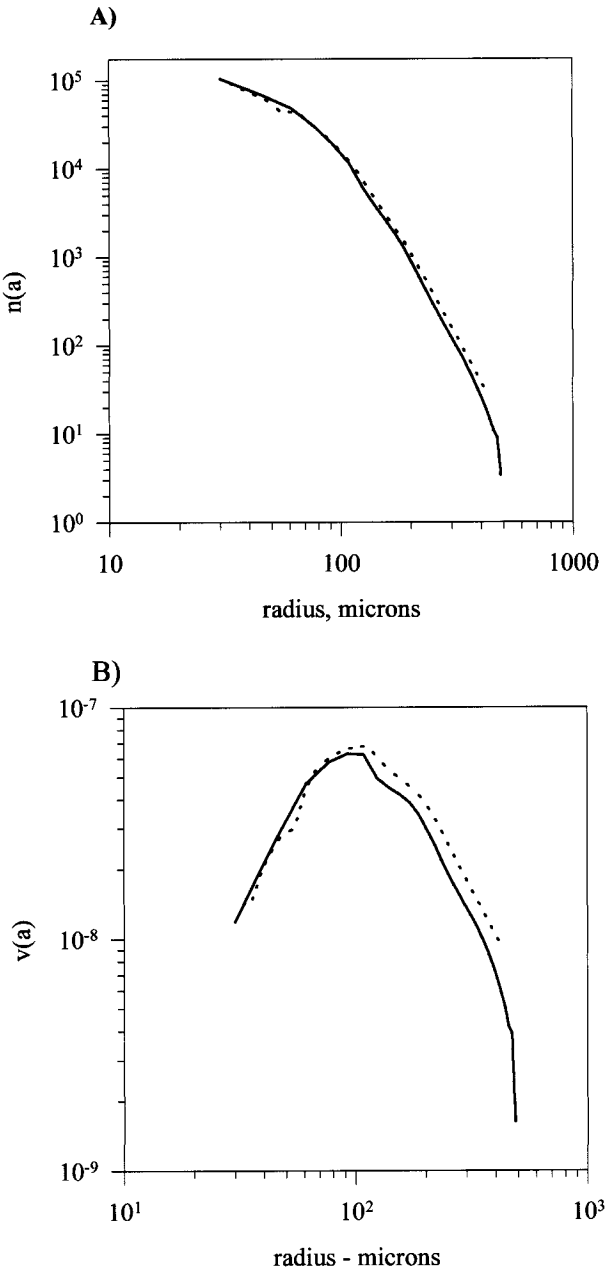

FIG. 10. (a) Example of the bubble size distribution calculated using both the resonant approximation (dashed line) (Wildt 1946) and the direct solution of Commander and McDonald (solid line) (1991) obtained 1 m downstream of the breaker at $t = 20$ s (refer to Fig. 7b). (b) The resulting bubble size distributions are scaled by their volume to arrive at the volume contribution by radius, $v(a)$. Note the tendency of the resonant approximation to overestimate the larger bubbles when compared with the method of Commander and McDonald (1991).

Implicit in the interpretation of the received acoustic signal is the assumption that the portion of the received signal due to scattering from bubbles outside the direct pathlength between the source and receiver are negligible compared to the forward transmitted signal. This can be shown by looking at the volume reverberation from a homogenous bubble population surrounding the bistatic sonar and showing that its level is much less than the direct signal emitted by the source. If we consider the intensity of the spherically spreading wave from the transmitter in an attenuating medium as

$$I(r) = \frac{I_0 \exp[-\eta(r - R_{1032})]}{r^2} \quad (15)$$

(η is the attenuation in Np m^{-1} and R_{1032} is the radius of the spherical source), it follows then that the scattering strength of some volume dV is

$$I_s(r) = \frac{I_0 \exp[-\eta(r - R_{1032})]M_v dV}{r^2}, \quad (16)$$

where M_v is the scattering cross section per unit volume, defined by

$$M_v = \int \sigma_s n(a)\, da = \int \frac{4\pi a^2 n(a)\, da}{\left[\left(\frac{\omega_0}{\omega}\right)^2 - 1\right]^2 + \delta^2}. \quad (17)$$

Note that the scattering cross section (σ_s) of a bubble at resonance is approximately an order of magnitude smaller than the extinction cross section [see Eqs. (18), (19)]. The intensity incident on the receiver (radius of R_{1042}) from the scattering volume dV is therefore

$$I_{\text{srcv}}(r) = \frac{I_0 \exp[-\eta(r - R_{1032})]M_v dV}{r^2} \frac{\exp[-\eta(r' - R_{1042})]}{r'^2}. \quad (18)$$

The distance r' from the receiver to dV is related to the distance r from dV to the source and the angle θ from the direct path (0° is aligned with l) by

$$r'^2 = l^2 + r^2 - 2lr\cos\theta. \quad (19)$$

To arrive at an equivalent plane wave reverberation level, Eq. (18) was numerically integrated using the 15-cm acoustic pathlength for a range of oceanic bubble densities (e.g., optical data of Johnson and Cooke 1979) and acoustic frequencies with the assumption that the scatterers near the source and receiver are homogenous. A 1-m^3 volume was used for integrating (18) despite the reverberation level typically reaching an asymptote at volumes two orders of magnitude smaller. The equivalent plane wave reverberation level calculated was then compared with the direct path intensity level [given by (15) at $r = 15$ cm] and found to be two to three orders of magnitude smaller. For example, the direct path signal was approximately 190 times larger for 32-μm bubbles ($f_r \sim 100$ kHz) with a density of 10^6 m^{-3} and approximately 1500 times larger for 100-μm ($f_r \sim 32$ kHz) bubbles with the same density. Calculations for the reverberation level that include the time dependence of the reverberation volume (see Clay and Medwin 1977) could also be performed with added complexity, due in part to the pulse length being almost seven times longer than the pathlength; however, the approach described above provides a conservative estimate for our purposes.

Spreading losses and variations in the acoustic pathlength due to vertical gradients in the sound were also examined using the Fermat principle and tracing rays between the source and receiver (Andersen and Kak 1982). Errors due to refractive effects were found to be minor for the 15-cm pathlength for expected vertical sound speed gradients in the upper ocean (see Terrill and Melville 1997a,b). In view of this and the calculations that suggest that off-axis bubble scattering plays a negligible role in modifying the transmitted signal, we estimate the effective sampling volume of the system to be a cylinder defined by the acoustic pathlength and a diameter of the receiver: approximately 140 cm^3.

4. Testing beneath laboratory generated breaking waves

a. Measurements

A series of experiments was performed in the large wind–wave channel at the Hydraulics Laboratory of Scripps Institution of Oceanography. The channel has dimensions of 45.6 m × 2.4 m × 2.4 m. A hydraulically driven wave generator resides at one end of the channel, while a beach of slope 1:8 at the other end dissipates the incident waves (see Fig. 6). The channel can be filled with seawater from pumps located on the end of Scripps Pier. Breaking waves were created by a technique adapted from the work of Rapp and Melville (1990), in which a packet of dispersive surface gravity waves is focused some distance downstream. At the focal point of the packet, the waves steepen and break. One benefit of using a mechanically generated breaking wave is that the wave packet is repeatable (Rapp and Melville 1990). Wave packets with a center frequency of 0.5 Hz (λ = 6.2 m) and a bandwidth of 0.8 Hz were chosen, as they provided a plunging breaker with a height of approximately 0.7 m. The amplitude and frequency of this two-dimensional breaker are similar to the scales of breaking wind waves in the field.

Acoustic measurements were made at a depth of 0.6 m at three separate locations: centered beneath the plume formed at the instant of breaking, and at stations 1 and 2 m downstream, as shown in Fig. 6. The broadband acoustic module spanned the centerline of the channel with the horizontal acoustic pathlength perpendicular to the propagation direction of the breaker. The acoustic module was left at a fixed location while a number of breaking waves were generated, typically pausing approximately 10 min between breakers. After 10 measurement runs at a fixed location, the module was moved to a downstream location. The repeatability of the breaker permits statistical comparisons from one location to another, despite the measured bubble fields originating from different breakers. Data were sampled continuously at a pulse rate of 5 Hz from the start of the generation of the wave packet and lasted for a number of minutes after the waves broke. Color time series (analogous to spectrograms), which show time on the x axis, frequency on the y axis, and attenuation or sound speed anomaly represented by a shade of color, are used

to present the large amounts of data analyzed. Figure 7 is an example of the measured broadband attenuation data collected at the three stations when a breaking wave was generated in seawater. The attenuation levels shown were calculated using the spectral approach described earlier. The time series of attenuation measured inside the young plume (Fig. 7a) appears quite short in duration, due to the advection of the bubble cloud past the fixed sensor. As the cloud advects and disperses, elevated levels of attenuation are recorded when the bubbles reach the acoustic modules downstream. The temporal variability in the broadband attenuation is quite apparent in the time series obtained at a fixed location. The spatial variability of bubble clouds generated by breaking waves is also quite evident if the measurements made at the various locations are compared. A consistent trend in the data is the reduction in attenuation levels as observations are made downstream from the breaker, with bubbles rising out of the water column as they advect downstream. It was found that the attenuation levels measured just beneath the breaker (Fig. 7a) exceeded the dynamic range of the system (Fig. 4c), and the levels shown at this station are saturated.

Like the color time series of the attenuation levels, the sound speed anomaly (defined as the sound speed in the mixture minus the bubble-free sound speed) can be assessed in a similar manner. Figures 8a,b present time series of the sound speed anomaly measured at the two downstream measurement locations, which were obtained from the same data used to produce the time series of attenuation shown in Figs. 7b,c. The time axis is expanded (and the frequency axis put in logarithmic scale) to show the structure of the measured dispersion within the bubble cloud at the two locations. Again, the variability in the bubble distribution produces fluctuations in the acoustical properties, as illustrated in the figure. The dispersive sound speed measured at a number of different times, indicated by the letters at the top of Fig. 8, are shown in Fig. 9. Note the similarities of the measurements to the modeled dispersion curves shown in Fig. 1c.

b. Analysis

The resonant approximation and the direct finite element bubble size inversion scheme of Commander and McDonald (1991) were applied to a portion of the data collected at the station 1 m downstream of the breaking wave. A 1-s average of acoustical data, obtained at $t =$ 20 s (see Figs. 7b and 8a), was used as input to the two inversion algorithms. Figure 10a is an example of the resulting bubble size distributions obtained from both techniques. The two are qualitatively similar, yet contain subtle differences. While it is known a priori that over a certain range of bubble sizes and frequencies (i.e., large bubbles and high frequencies) the resonant approximation will introduce errors (Commander and Moritz 1989), it appears that for this particular range of frequencies and bubble densities that the errors are not appreciable when compared to the results based on the method developed by Commander and McDonald (1991). The contribution of bubble radius to the total void fraction (Fig. 10b) is obtained by scaling the number of bubbles by their volume:

$$v(a) = \frac{4}{3}\pi a^3 n(a). \tag{20}$$

The curves illustrate the tendency of the resonant approximation (dotted line) to overestimate the number of larger bubbles (Commander and Moritz 1989) when compared to the direct method of Commander and McDonald (1991) (solid line). Due to the direct approach in solving the integral Eq. (9) and the fast computational speed, we use their method for further inversions of the data obtained by the broadband pulse technique.

Acoustic data obtained at the downstream stations are inverted for bubble sizes. Referring to Fig. 7b, data obtained from the station located 1 m downstream of the breaker are inverted on a per-ping basis using the Commander and McDonald (1991) approach for the period of time $t =$ 18–42 s and the resulting size distributions are shown in Fig. 11a. The scatter in the data is a reflection of the variability of the size distribution within the bubble cloud. Figure 11b presents four selected size distributions that display the variability in the distributions as the collection of bubbles advect past the acoustic module.

An optical bubble counting technique was operated (by Peter Geissler) at the same 1 m downstream location as the broadband module, providing an independent check on the acoustic sizing of the bubbles. The instrument, developed by Geissler and Jahne (1997a,b), is a high-resolution optical technique that records images of bubbles passing through a carefully calibrated sampling volume. Automated image processing techniques are used to create histograms of the bubble sizes as measured over a number of images. While optical data were not sampled concurrently with the acoustical data, the statistical repeatability of the breaking wave provides the ability to compare the measurements. Six seconds of data composed of 180 images were analyzed to arrive at the distribution, which is represented by the open squares in Fig. 11a. The optical data lie within the scatter of the acoustically derived distributions, demonstrating the accuracy of the acoustic data and its subsequent inversion.

The mean size distribution of bubbles for the 1- and 2-m downstream measurement locations, calculated after inverting the acoustic data on a per-ping basis (ping rate 5 Hz), are shown in Fig. 12a. The downstream distributions are based upon the data spanning $t =$ 18–42 s and $t =$ 31–50 s in Figs. 7b,c, respectively. Figure 12b shows the volume-scaled mean size distributions corresponding to Fig. 12a. The curves reveal that bub-

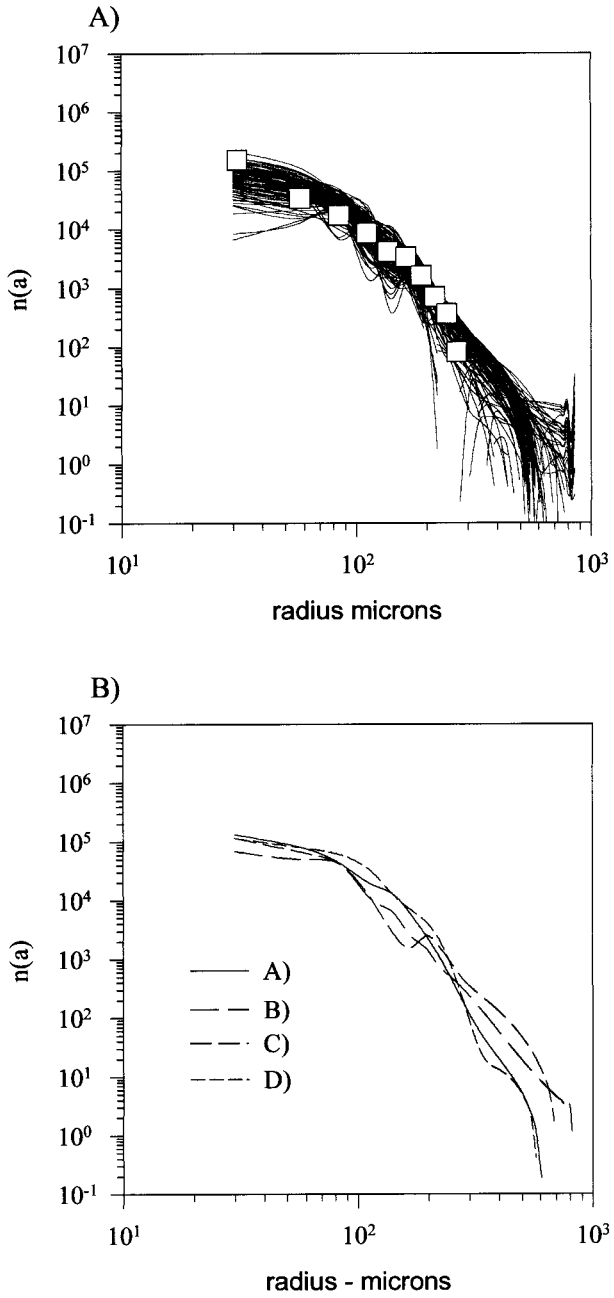

FIG. 11. (a) Bubble size distributions that result from inverting acoustic attenuation spanning the period of time (t = 18–42 s) when the bubble plume advects past the sensor. Attenuation data obtained at 5 Hz were inverted on a per-ping basis to arrive at the 120 distributions shown. The attenuation data used are those shown in Fig. 5b. The hollow square symbols represent the size distribution obtained from an optical technique used at the same location downstream from the breaking wave. (b) Examples of four bubble size distributions from (a) that show the variability in $n(a)$ when the bubbles pass through the pathlength of the broadband sound speed module.

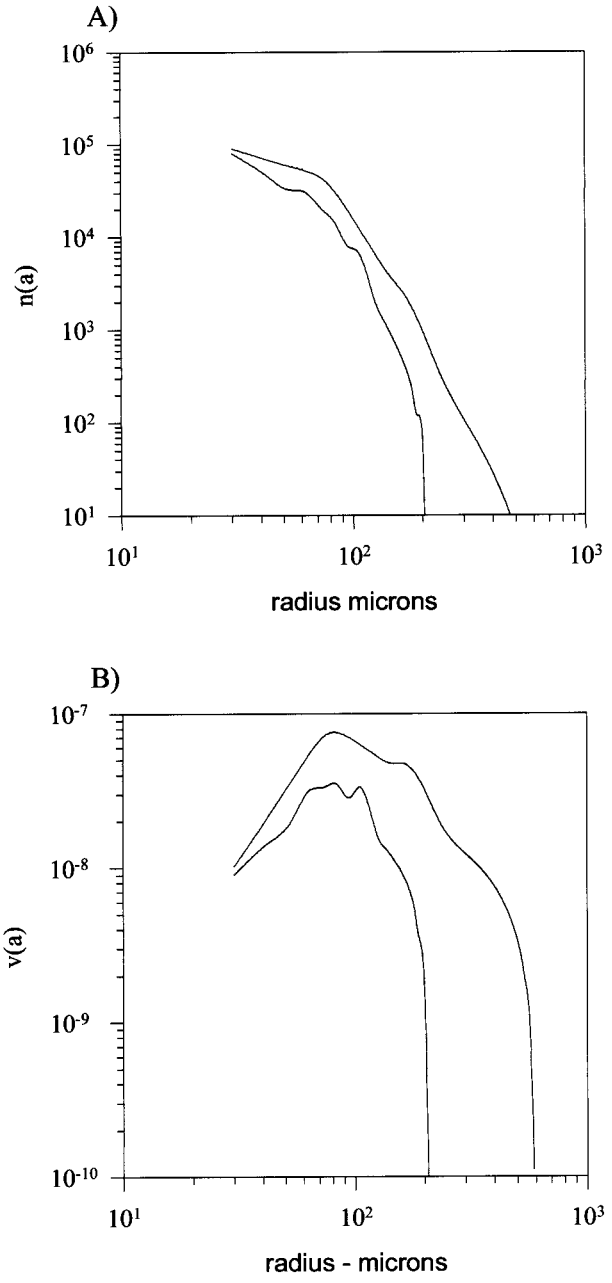

FIG. 12. (a) The mean bubble size distributions and (b) the resulting mean volume scaled distributions for the 1- (solid) and 2-m (dashed) downstream measurement locations. Each mean is calculated using $O(100)$ size distributions that were inverted on a per-ping basis for t = 18–42 s and t = 31–50 s at the two locations. The upper solid line is the 1-m downstream location and the lower solid line is the 2-m downstream location. The volume-scaled distribution reveals that bubbles with radii ranging from 60–90 μ (resonant frequencies of 36–54 kHz) contribute most to the void fraction at these locations. Note the similarities in numbers of small bubbles and the differences for the larger bubbles for the two measurement locations. This is attributed to the larger bubbles rising out of solution faster.

bles with radii in the range of 60–90 μ contribute most to the total void fraction. This corresponds to a peak in the acoustic attenuation at frequencies of 36–54 kHz. While similar numbers of bubbles exist at the smaller radii, there appear to be significant differences in the number of larger bubbles. This is not unreasonable considering that for this range of bubble sizes, the rise velocity of the bubbles is proportional to the square of the radius (Clift et al. 1978), forcing the larger bubbles to reach the surface at a significantly faster rate. For example, the terminal rise velocity of an air bubble with a 30-μm radius is 0.08 cm s^{-1}, while the rise velocity for an 800-μm air bubble is approximately 30 cm s^{-1}, an increase of over 350 times.

As mentioned earlier, the fact that the broadband technique is capable of measurements of both sound speed and attenuation permits tests of the internal consistency of the measurements. Once the bubble size distribution is known, the real and imaginary parts of the complex dispersion relation [Eq. (2)] can be calculated. Hence, inverting the attenuation data (imaginary part) for the size distribution allows the subsequent calculation of the sound speed (real part). Figure 13 shows a number of example dispersion curves for both measured (solid line) and calculated (dashed line) sound speeds for a number of bubble size distributions representative of the range of void fractions entrained in the laboratory breaking wave experiments. A further check on the quality of the bubble size data is to calculate the resultant void fraction, given by

$$\beta = \frac{4}{3}\pi \int a^3 n(a)\, da, \tag{21}$$

where $n(a)$ is the size distribution obtained from inverting the attenuation data. The void fraction of the mixture can also be calculated using Wood's relation [Eq. (3a)] and the lowest frequency (4 kHz) measured sound speed. Figure 13 lists the values of the void fractions obtained by both these methods for the data shown in the figure. The differences between these values may be attributed to the 4-kHz sound speed not completely satisfying the nondispersive assumption for certain bubble size distributions with large bubbles present whose resonant frequency is below that which is measured.

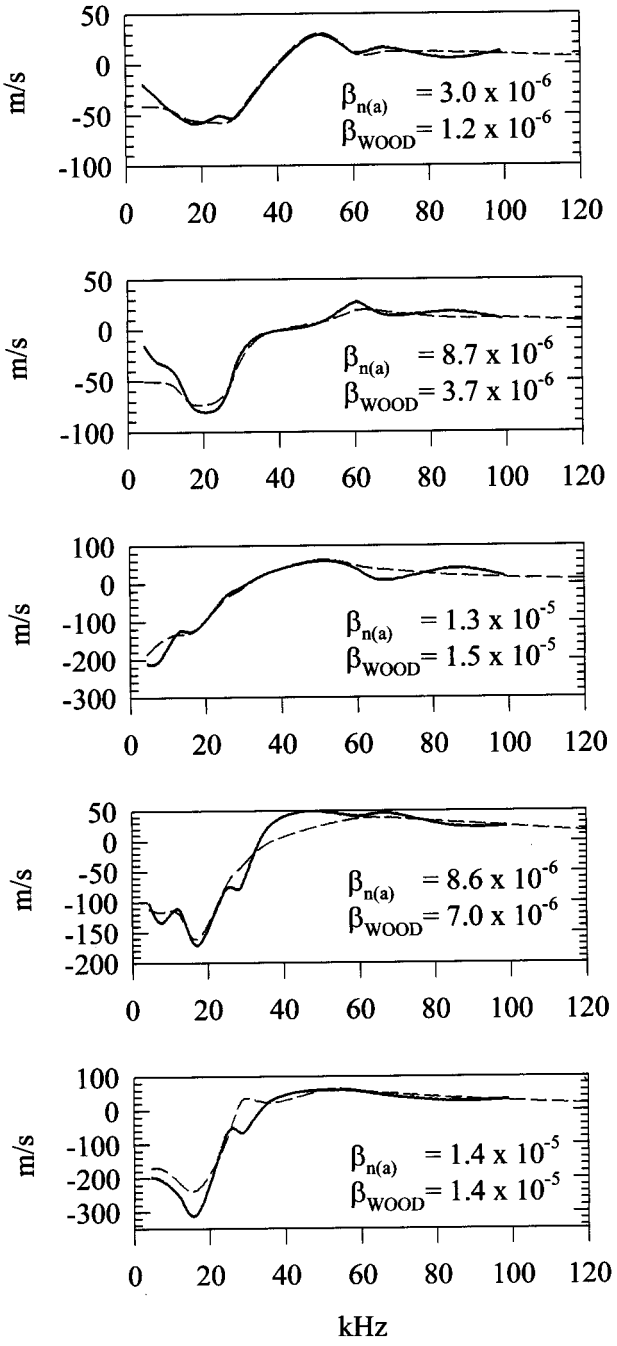

FIG. 13. Five representative internal consistency checks performed on single-ping acoustic data using sound speed and attenuation data. The solid lines represent the measured sound speed and the dashed lines represent the sound speed calculated using the bubble size distribution obtained from inverting the attenuation. Also shown are the void fractions calculated via Wood's relation and the 4-kHz sound speed data (β_{WOOD}) and the void fraction obtained by integrating over the bubble size distribution ($\beta_{n(a)}$). The void fractions shown range from $O(10^{-6})$ to $O(10^{-5})$ and are representative of the concentrations produced in the laboratory experiments downstream of the breaker.

5. Shallow water measurements

A field experiment designed to characterize nearshore bubble size distributions and measure their effects on underwater sound propagation was performed from 1–12 March 1997 near the Scripps Pier in La Jolla, California. The multi-investigator experiment also had participants from the Naval Research Laboratory; the Institute of Ocean Sciences (Canada); the Applied Physics Laboratory, University of Washington; and the National Center for Physical Acoustics. While a comprehensive description of the results of the field experiment is outside the scope of this paper, we present a few

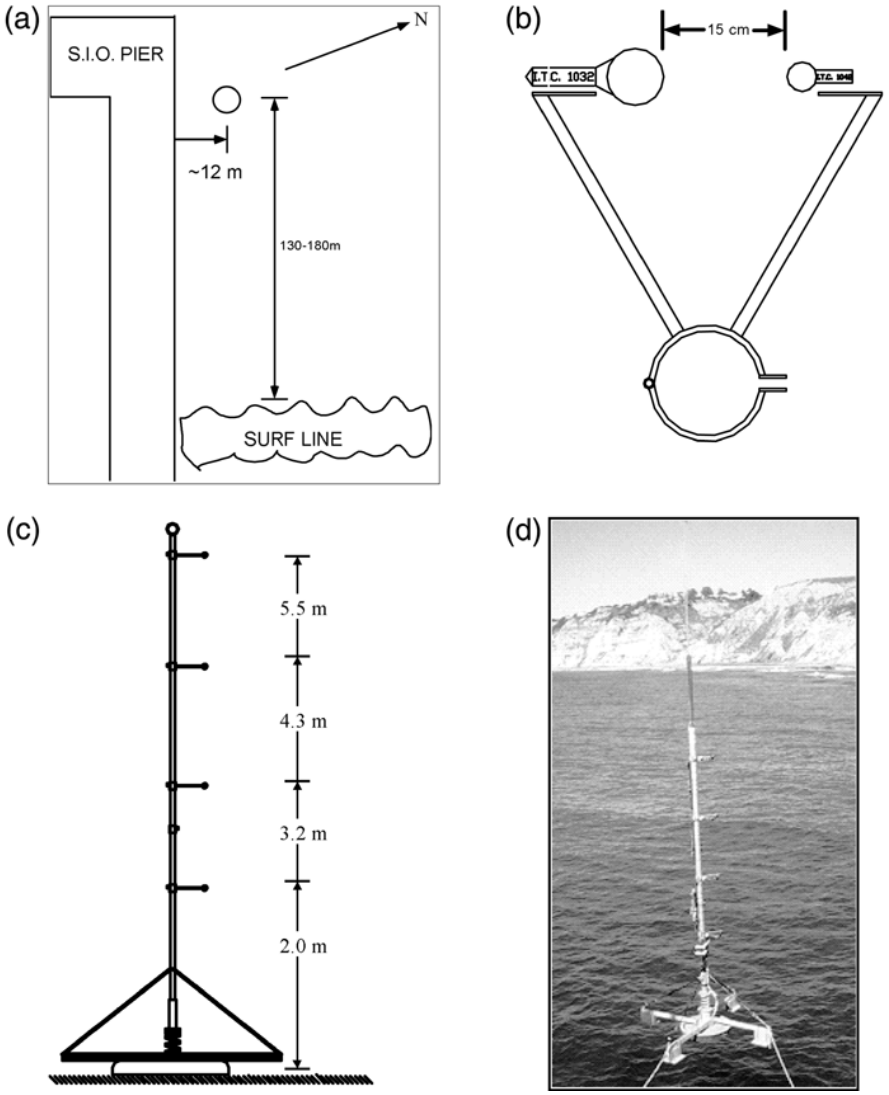

FIG. 14. Overview of the equipment used in obtaining shallow water measurements in Mar 1997. (a) Plan view of the location of the vertical array of sound speed modules with respect to Scripps Pier and the surf line. (b) Schematic of the sound speed module mounted to vertical spar. (c) Schematic of the vertical array showing distances measured from the base of the spar. A compliant base was used to allow the vertical spar to move under heavy waves to minimize high stresses. The array of modules were deployed in water of nominal 6-m depth. (d) Photograph of the system being deployed from Scripps Pier.

→

FIG. 15. Time series of attenuation measured near the end of Scripps Pier. The data show an ''event'' of high attenuation levels measured at (a) 1.1-, (b) 2.2-, and (c) 3.4-m depth. The high levels of attenuation are due to bubbles advecting offshore in rip currents. Note the vertical gradient in the attenuation level observed. This particular event appears to be $\approx$ 25 s in duration. Current measurements at the spar showed the offshore velocity component to be $\approx$ 25 cm s^{-1}, resulting in a cross-shore length scale of the bubble cloud to be roughly 8 m. Color time series of the bubble size distribution are obtained by inverting the attenuation data shown in (a)–(c) for the three different depths using the Commander and McDonald (1991) algorithm and shown in (d)–(f). The color scale is the logarithm of the number density to accommodate the large dynamic range of bubbles present. The horizontal line at $a = 40$ μm is due to electrical noise in the system.

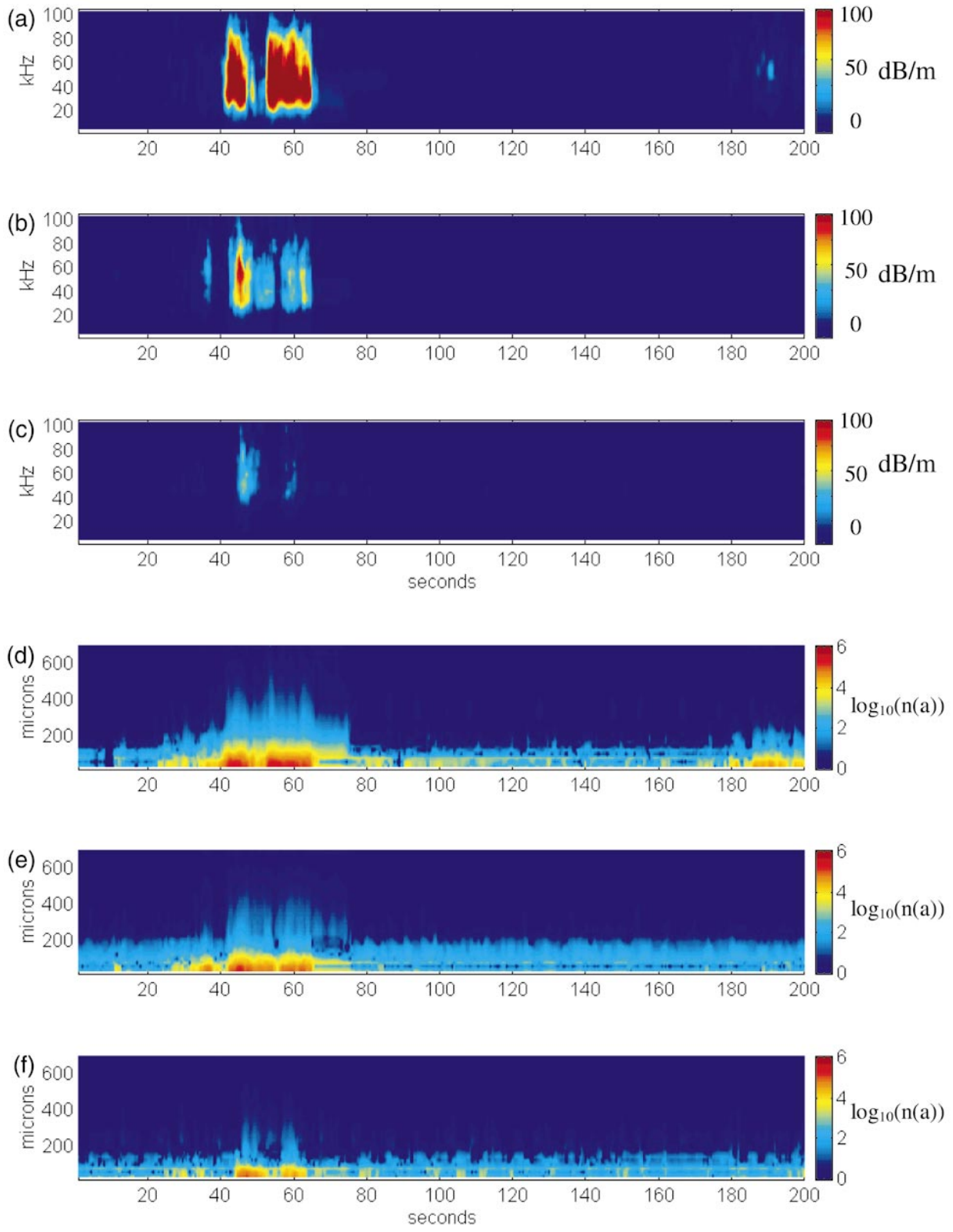

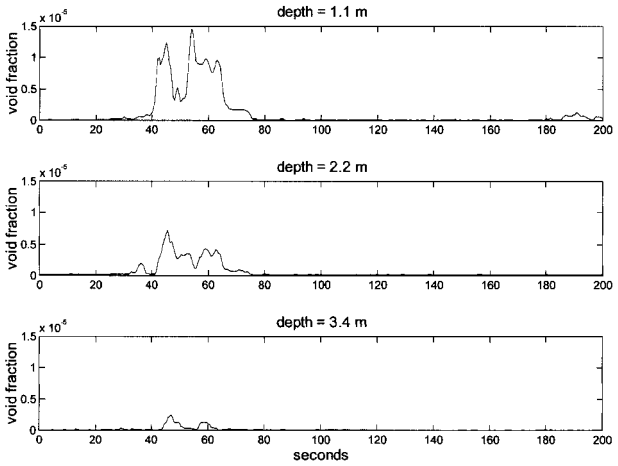

FIG. 16. Time series of the void fraction measured at (a) 1.1-, (b) 2.2-, and (c) 3.4-m depth for the period of time shown in Fig. 15. Void fractions measured during the passage of the bubble cloud are $O(10^{-5})$.

examples to illustrate the application of the technique for field measurements. The broadband technique was employed in a field-deployable system composed of a vertical array of four modules, mounted to a 6-m-long aluminum spar at distances of 2, 3.2, 4.3, and 5.5 m from the base. The transmit and receive transducers were aligned with a horizontal pathlength of 15 cm. The spar was mounted to a railcar wheel via a semicompliant base, which allowed some horizontal displacement to reduce loads in large waves. The array was mounted approximately 12 m north of the Scripps Pier in water of a nominal depth of 6 m. Figure 14 presents a description of the deployment location, schematics of both the broadband modules and the vertical array, as well as a photograph of the system being deployed from Scripps Pier.

Cables from the transmit and receive transducers were connected to two pressure cases mounted at the base of the spar. The pressure cases connected the cables from the modules to two multiconductor waterproof cables, which were subsequently connected to the remainder of the hardware (Fig. 3) in a small laboratory at the end of the pier. The pressure case belonging to the receiving side of the array housed preamps to compensate for signal attenuation in the cable run. The ping rate for the field system was 2 Hz for each individual module.

Figure 15 presents a portion of the data collected on the afternoon of 8 March 1997. Several rip currents, visible from the surface by the entrained bubbles and sediment, were observed to pass through the area of the vertical array during the spring low tide that coincided with this period of time. Current measurements, made near the array using an electromagnetic current meter mounted 1 m above the seafloor, showed an offshore flow of approximately 25 cm s^{-1} associated with the rip currents. Figures. 15a–c show color time series of the attenuation measured at depths of 1.1, 2.2, and 3.4 m.

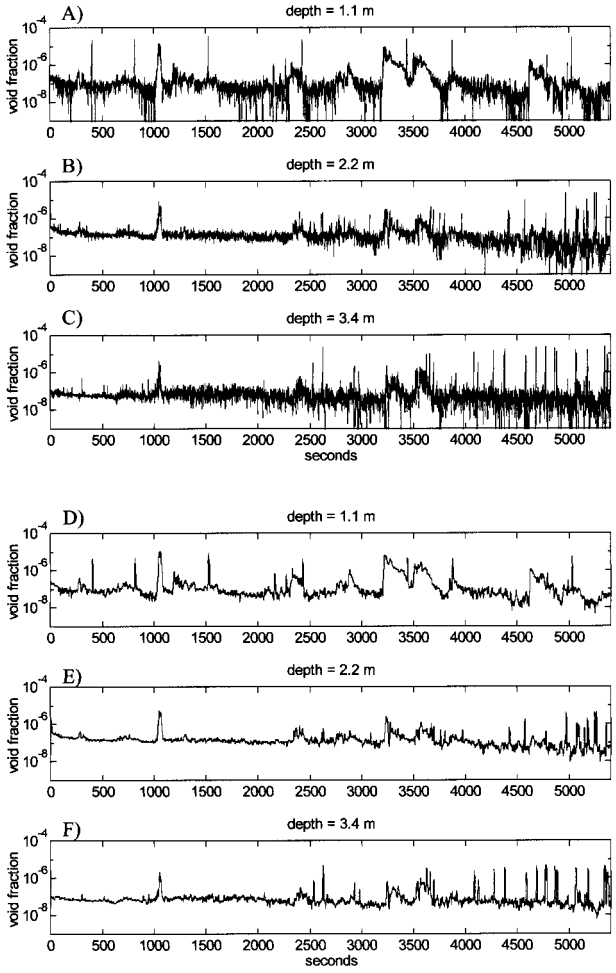

FIG. 17. Time series of the void fraction present in the water column at depths of (a) 1.1, (b) 2.2, and (c) 3.4 m measured for 1.5 h during the afternoon of 8 Mar 1997. Each data point is obtained by integrating the resulting bubble size distribution obtained from the attenuation data measured at a 2-Hz rate. The color time series of attenuation, bubble size distributions, and void fractions shown in Figs. 15 and 16 represent the event starting at $t = 1000$ s. A logarithmic scale is used for the void fraction. The time series shown in (d)–(f) are the same except for the application of a running mean smoothing filter (5-s window) to the data. The data show several events of high levels of void fraction with varying time scales and vertical dependence.

The shallowest broadband module was at or above the water surface due to the low tide and provided no data during this period of time.

The time series reveal a significant increase in the acoustic attenuation, approaching levels of 100 dB m^{-1}, during the time $t = 40$–70 s. High coherences were found between the various measurement depths despite the vertical gradient in the levels measured. The attenuation data are inverted for bubble size distributions using the Commander and McDonald (1991) method and presented as a color time series in Figs. 15d–f. The x axis is time in seconds, the y axis is bubble radius in microns, and the color intensity is the logarithm of the

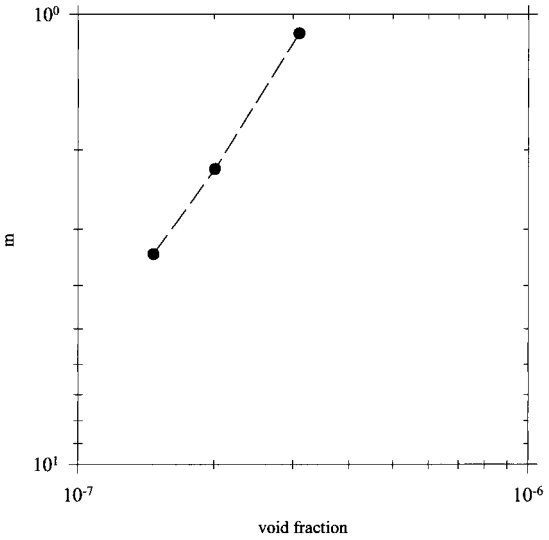

FIG. 18. The depth dependence of the mean void fraction calculated from the 1.5 h of data shown in Fig. 17. The depth dependence appears to follow a power-law relationship with a slope of approximately −1.5.

number density in units of number per m^3 per micron increment. The logarithm of the number density is used because of the large dynamic range (approximately six orders of magnitude) in the number of bubbles present. The data show that high concentrations of bubbles are present during this particular event. The horizontal lines in the distributions are the effects of low-level electrical noise on the low bubble density performance of the instrument. For example, the line at $a = 40$ μm, corresponding to a resonant frequency of approximately 80 kHz, appears to have a value of $O(10^3)$. If we consider that the minimum attenuation level the system can measure at this frequency (Fig. 4c) is 0.7 dB m^{-1} and apply it to the resonant approximation inversion, the number density calculated is in agreement to the levels shown. Time series of the void fraction, calculated by integrating the size distribution of bubbles [Eq. (21)], are shown in Figs. 16a–c for the three measurement depths. The 2-Hz sampling rate appears to provide adequate temporal resolution for measurement of the fine structure found in the event.

Variability in the field data is clearly revealed in longer time series of void fraction for 1.5 h of data obtained during that same afternoon, as shown in Fig. 17. (Note that $t = 0$ s in the previous figures corresponds to $t = 1000$ s in this figure.) While a logarithmic scale is required to display the dynamic range of the void fractions, the scale also emphasizes the low void fraction variability that is a combination of the effects of electrical noise on the system (Fig. 5b) and the bubble statistics that will depend on the flow conditions and bubble concentrations. A running mean filter with a 5-s window is applied to the data to emphasize the eventlike structure of the void fraction field and remove the low level ''noise.'' The filtered time series are shown in Figs. 17d,e. Testing of window lengths indicated that a 5-s window removed much of the short timescale variability, providing a ''smoother'' time series that retained the longer timescale events. The smoothing appears asymmetric in its removal of the spikes toward low void fraction because of the logarithmic scale. The data show void fractions ranging from 10^{-8} to over 10^{-5} for the 1.5 h of data. While the bubble field is bound to be variable, a portion of the variability in the shallow water data obtained is attributed to the advection of the bubble field past the sensor by the orbital velocities of the waves and by movement of the spar. This was revealed by local peaks in the spectra of the void fraction time series coinciding with peaks in the spectra of surface gravity wave field. It is important to recognize that a portion of the variance of the signal measured can be attributed to spatial variations advecting past the sensor.

The long time series also reveals varying degrees of vertical coherence from one event to another, emphasizing the need for measurements at multiple depths if measuring bubble concentrations. The mean void fraction depth dependence, calculated using void fractions measured at the 2-Hz rate for the three measurement depths, is found to follow a power-law relation with a slope of −1.5 (Fig. 18) for the 1.5 h of data shown in Fig. 17.

6. Conclusions

A new instrument has been developed that is able to directly measure the sound speed and attenuation over a wide range of frequencies. The resulting acoustic data are inverted for bubble size distributions using the method developed by Commander and McDonald (1991). The acoustic system measures the sound speed and attenuation at sampling rates up to 12 Hz, providing the capacity to measure the bubble size distributions with good temporal resolution. The system measures attenuation levels from less than 1 dB m^{-1} to several hundred dB m^{-1}, which corresponds to a wide dynamic range of void fractions. The ability to measure both the real and imaginary parts of the complex dispersion relationship permits internal consistency checks to be performed on the acoustic data. The system was tested in bubble clouds generated by laboratory breaking waves in seawater and found to give good agreement with an independent optical bubble counting technique.

A four-channel array of broadband modules was deployed in shallow water near the Scripps Pier. Concentrations of bubbles from breaking waves in the surf zone were observed to advect past the vertical array. Attenuation levels measured were found to approach $O(100)$ dB m^{-1} (similar in magnitude to those measured in the laboratory). The temporal variability and vertical gradients in the bubble size distribution indicate the need for field measurements to be performed over a wide range of conditions and depths. It is expected that further

studies using the described acoustic technique will provide valuable insight into the nature of the size distributions of bubbles in the ocean.

Acknowledgments. We wish to thank the staff of the Hydraulics Laboratory at SIO, including David Aglietti, Charles Coughran, and John Lyons, for help in preparing the wave channel for the breaking wave measurements. Peter Geissler and Bernd Jahne are thanked for providing the optical measurements of bubble size distributions in the laboratory experiments. We also thank Kerry Commander of the Coastal Systems Station for providing his bubble size inversion code. Peter Matusov, Mike Ritter, and Fabric Veron are thanked for their help in the deployment and recovery of the acoustic instrumentation in the shallow water field experiment. The development of the instrumentation was funded by National Science Foundation (Ocean Instrumentation), and the Scripps Pier Experiment was funded by ONR (Acoustics).

REFERENCES

Akulichev, V. A., V. A. Bulanov, and S. A. Klenin, 1986: Acoustic sensing of gas bubbles in the ocean medium. *Sov. Phys. Acoustic.*, **32** (3), 177–180.

Andersen, A. H., and A. C. Kak, 1982: Digital ray tracing in two-dimensional refractive fields. *J. Acoust. Soc. Amer.,* **72,** 1593–1606.

Blanchard, D. C., and A. H. Woodcock, 1957: Bubble formation and modification in the sea and its meteorological significance. *Tellus*, **9,** 145–158.

Clay, C. S., and H. Medwin, 1977: *Acoustical Oceanography*. John Wiley and Sons 544 pp.

Clift, R., J. R. Grace, and M. E. Weber, 1978: *Bubbles, Drops, and Particles*. Academic Press 380 pp.

Commander, K. W., and E. Moritz, 1989: Off-resonant contributions to acoustical bubble spectra. *J. Acoust. Soc. Amer.,* **85,** 2665–2669.

——, and A. Prosperetti, 1989 Linear pressure waves in bubbly liquids: Comparison between theory and experiments. *J. Acoust. Soc. Amer.,* **85,** 732–746.

——, and R. J. McDonald, 1991: Finite-element solution of the inverse problem in bubble swarm acoustics. *J. Acoust. Soc. Amer.,* **89,** 592–597.

Devin, C., 1959: Survey of thermal, radiation and viscous damping of pulsating air bubbles in water. *J. Acoust. Soc. Amer.,* **31,** 1654–1667.

Duraiswaimi, R., 1993: Bubble density measurement using an inverse acoustic scattering technique. *ASME Cavitation and Multiphase Flow Forum,* New York, NY, ASME, 67–74.

Farmer, D. M., and S. Vagle, 1989: Waveguide propagation of ambient sound in the ocean surface bubble layer. *J. Acoust. Soc. Amer.,* **86,** 1897–1908.

——, and ——, 1997: Bubble measurements using a resonator system. *Natural Physical Processes Associated with Sea Surface Sound,* T. G. Leighton, Ed., University of Southampton 155–162.

Feuillade, C., 1996: The attenuation and dispersion of sound in water containing multiply interacting air bubbles. *J. Acoust. Soc. Amer.,* **99,** 3412–3430.

Foldy, L. L., 1945: The multiple scattering of waves. *Phys. Rev.,* **67,** 107–119.

Fox, F. E., S. R. Curley, and G. S. Larson, 1955: Phase velocity and absorption measurements in water containing air bubbles. *J. Acoust. Soc. Amer.,* **27,** 534–546.

Geissler, P., and B. Jahne, 1997a: A 3D. sensor for the measurement of particle concentration from image sequences. *Int. Archives of Photogrammetry and Remote Sensing,* Vienna, Austria, Committee of the XVIII Int. Congress for Photogrammetry Remote Sens.

——, and ——, 1997b: Laboratory and inshore measurements of bubble size distributions *Natural Physical Processes Associated with Sea Surface Sound,* T. G. Leighton, Ed., CBC Print and Media Resources 147–154.

Johnson, B. D., and R. C. Cooke, 1979: Bubble populations and spectra in coastal waters: A photographic approach. *J. Geophys. Res.,* **84,** 3761–3776.

Kerman, B. R., 1988: *Sea Surface Sound: Natural Mechanisms of Surface Generated Noise in the Ocean.* Kluwer Academic Publishers 639 pp.

——, 1993: *Natural Physical Processes Associated with Sea Surface Sound.* Kluwer Academic Publishers 750 pp.

Kolaini, A. R., 1997: Effects of salt on bubble radiation. *Natural Physical Processes Associated with Sea Surface Sound,* Leighton, T. G. Ed., CBC Print and Media Resources 240–249.

Kolovayev, D. A., 1976: Investigation of the concentration and statistical size distribution of wind-produced bubbles in the near-surface ocean. *Oceanology,* **15,** 659–661.

Lamarre, E., and W. K. Melville, 1994: Sound speed measurements near the ocean surface. Instrumentation for the measurement of sound speed near the ocean surface. *J. Acoust. Soc. Amer.,* **96,** 3605–3616.

——, and ——, 1995: Instrumentation for the measurement of sound speed near the ocean surface. *J. Atmos. Oceanic Technol.,* **12,** 317–329.

Leander, J. L., 1994: Transient wave propagation through bubbly layers via the Foldy–Twersky integral equation. *J. Acoust. Soc. Amer.,* **95,** 2378–2386.

Leighton, T. G., 1994: *The Acoustic Bubble.* Academic Press 613 pp.

Medwin, H., 1970: In situ acoustic measurements of bubble populations in coastal waters. *J. Geophys. Res.,* **75,** 599–611.

——, 1975: Speed of sound in water: A simple equation for realistic parameters. *J. Acoust. Soc. Amer.,* **58,** 1318–1319.

——, 1977: In situ acoustic measurements of microbubbles at sea. *J. Geophys. Res.,* **82,** 971–976.

——, and N. D. Breitz, 1989: Ambient and transient bubble spectral densities in quiescent seas and under spilling breakers. *J. Acoust. Soc. Amer.,* **88,** 408–412.

——, J. Fitzgerald, and G. Rautman, 1975: Acoustic miniprobing for ocean microstructure and bubbles. *J. Geophys. Res.,* **80,** 405–413.

Melville, W. K., E. Terrill, and L. Ding, 1995: Field measurements of air entrainment by breaking waves. *Proc. of the Third Int. Symp. on Air–Water Gas Transfer,* B. Jahne, Ed., Springer Verlag 285–295.

——, ——, and F. Veron, 1997: Bubbles and turbulence under breaking waves. *Natural Physical Processes Associated with Sea Surface Sound.* T. G. Leighton, Ed., University of Southampton, 135–145.

Pace, N. G., A. Cowley, and A. M. Campbell, 1997: Short pulse acoustic excitation of microbubbles. *J. Acoust. Soc. Amer.,* **102,** 1474–1479.

Quazi, A. H., 1981: An overview on the time delay estimate in active and passive systems for target localization. *IEEE Trans. ASSP,* **29,** 527–533.

Rapp, R. J., and W. K. Melville, 1990: Laboratory measurements of deep-water breaking waves. *Philos. Trans. Roy. Soc. London,* **331A,** 735–800.

Silberman, E., 1957: Sound velocity and attenuation in bubbly mixtures measured in standing wave tubes. *J. Acoust. Soc. Amer.,* **29,** 925–933.

Su, M.-Y., D. Todoroff, and J. Cartmill, 1994: Laboratory compari-

sons of acoustic and optical sensors for microbubble measurement. *J. Atmos. Oceanic Technol.*, **11,** 170–181.
Suiter, H. R., 1992: Pulse length effects on the transmissivity of bubbly water. *J. Acoust. Soc. Amer.*, **91,** 1383–1387.
Terrill, E. J., 1998: Acoustic measurements of air entrainment by breaking waves. Ph.D. dissertation, Scripps Institution of Oceanography, University of California, San Diego 244 pp. [Available from University of California, San Diego, La Jolla, CA 92093.]
——, and W. K. Melville, 1996: A broadband acoustic technique for measuring bubble size distributions. *J. Acoust. Soc. Amer.*, **100,** 2840–2841.
——, and ——, 1997a: Sound speed measurements in the surface-wave layer. *J. Acoust. Soc. Amer.*, **102,** 1–19.
——, and ——, 1997b: High frequency acoustics in shallow water. Lerici, Italy, NATO SALLANT.
——, and ——, 1998: Bubbles and surf zone oceanography. *J. Acoust. Soc. Am.,* **103,** 2828–2829.
Vagle, S., and D. M. Farmer, 1998: A Comparison of four methods for bubble size and void fraction measurements. *IEEE J. Ocean Eng.,* **23,** 211–222.
Waterman, P. C., and R. Truell, 1961: Multiple scattering of waves. *J. Math Phys.,* **2,** 512–537.
Wildt, R., 1946: Acoustic theory of bubbles. *Physics of Sound in the Sea,* Vol. 8, Department of Defense 546 pp.
Wood, A. B., 1941: *A Textbook of Sound.* G. Bell and Sons 578 pp.